European Geothermal Congress 2016
Strasbourg, France, 19-24 Sept 2016

Automatic pressure control in enhanced geothermal systems*

Moritz Schulze Darup[1] and Jörg Renner[2]

[1]Control Group, Department of Engineering Science, University of Oxford, United Kingdom

[2]Experimental Geophysics, Department of Geoscience, Ruhr-Universität Bochum, Germany

moritz.schulzedarup@rub.de

Keywords: Enhanced geothermal systems (EGS), hydraulic stimulation, model predictive control (MPC), unscented Kalman filter (UKF).

ABSTRACT

We present an automatic control scheme to regulate the fluid pressure in the reservoir rock of deep geothermal systems. Controlling the fluid pressure profile is important to avoid strong seismic events during hydraulic stimulation. The proposed feedback controller uses a model describing the pressurization and seismicity in the reservoir to predict the future system behavior. The prediction requires the knowledge of (an estimation of) the current system state. Since direct measurements of system states are limited, we additionally design an unscented Kalman filter to solve the observation problem.

1 INTRODUCTION

Geothermal systems become more and more important for the generation of electrical energy. The total worldwide installed capacity of geothermal power plants currently is 12.635 GW with an increase of about 350 MW per year (see (Bertani, 2015) for details). Geothermal power plants are, in general, environmentally friendly. However, the development of enhanced geothermal systems (EGS, see Fig. 1) requires to artificially increase the permeability in the reservoir rock such that water can circulate. The permeability increase is effectuated by hydraulic stimulation that causes seismic activity. While the magnitudes of the induced seismic events are typically small, strong events were recognized during hydraulic stimulations and even during geothermal circulation (see, e.g., Tab. 1 further below, McGarr (2014), or Evans et al. (2012)). Although such induced seismicity is usually short lived, the activities in Landau, Soultz-sous-Forêts, and Basel have raised public concern due to their proximity to populated areas. The goal is thus to safely develop an EGS without provoking massive seismicity.

In this paper, we introduce a feedback control scheme to automatically regulate the fluid pressure profile in the reservoir rock of an EGS. In principle, the fluid pressure in the reservoir can be controlled by adapting the fluid flow in two wells (that, during power plant operation, will serve as injection and production well as sketched in Fig. 1). The pressurization in the reservoir will be delayed and alleviated due to diffusion processes. A reliable controller thus has to take the future system behavior into account. Model predictive control (MPC, see Rawlings and Mayne (2009) for an overview) schemes, which are well known in the field of control engineering, cope with this requirement. Model predictive controllers use a mathematical model of the system to predict the future behavior for different control actions (here fluid flow in the wells). The optimal control action is then identified based on a predefined performance index. Finally, to account for model uncertainties and unmodelled disturbances, the optimal control sequence is applied to the system only for a fixed time span and the procedure (i.e., prediction and optimization) is repeated afterwards. This strategy incorporates feedback into the control scheme.

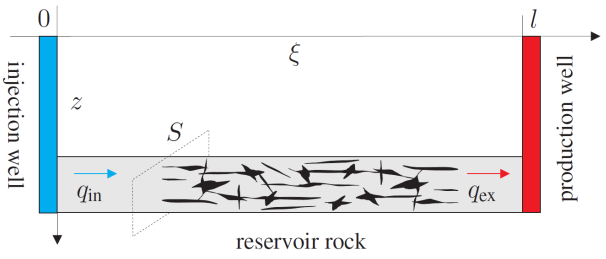

Figure 1: Schematic illustration of an enhanced geothermal system.

Model predictive control is appealing since it can be formulated as an optimal control problem (OCP), which can be efficiently solved using numerical optimization. However, the repeated solution of the underlying optimal control problem (OCP) requires the knowledge of (an estimation of) the current system state. Since it is not possible to completely measure the system state of the EGS (including space- and time-resolved pressures, permeabilities, and stresses), the design of a so-called state observer is required. The design of the observer is demanding since the derived model of the EGS is nonlinear, uncertain, and non-differentiable. We thus implement an unscented Kalman Filter (UKF, see Julier and Uhlmann (1997)), which can handle such complex models.

*This article is an extended version of the paper (Schulze Darup and Renner, 2016) presented at the European Control Conference 2016. In particular, we detailed the description of the control scheme and modified the presentation to better address the geothermal community.

Table 1: Maximum magnitudes of earthquakes induced by fluid injection at geothermal sites.

Location		Magnitude	Year	Reference
Landau	(Germany)	2.7	2009	Bönnemann et al. (2010)
Soultz-sous-Forêts	(France)	2.9	2003	(McGarr, 2014, Tab. 1)
Basel	(Suisse)	3.4	2006	(McGarr, 2014, Tab. 1)
Cooper Basin	(Australia)	3.7	2003	(McGarr, 2014, Tab. 1)
Berlín Field	(El Salvador)	4.4	2003	(Baisch et al., 2010, Tab. 1)

Controlling the pressure profile is the key to managing the induced seismicity. We stress, however, that the presented method is not yet capable of directly regulating the seismicity. The procedure to be presented should thus be understood as preparatory work for a more complex predictive control scheme explicitly including the induced seismicity. Control schemes for the automatic regulation of seismic activity in EGS are rare. To the best of our knowledge, the only method documented in the literature is the traffic-light system proposed in Bommer et al. (2006). The method was tentatively applied during hydraulic stimulations in Berlín (El Salvador) and Basel (see Sect. 3.2 in Häring et al. (2008)) to avoid massive seismic events. The application of the proposed scheme is complicated, however, since transitions between the different operation modes (i.e., green light or red light) are not well-defined (see Sect. 3.1 in Gaucher et al. (2015)). Moreover, a forecast of the induced seismicity is not included in the approach.

The paper is organized as follows. In Section 2, we introduce a rudimentary model (that is inspired by Baisch et al. (2010)) describing the pressurization and seismic activity in an EGS. We analyze the derived model in Section 3 and show that elementary characteristics of an EGS are reproduced by the model. The main result of the paper, i.e., the predictive pressure control and state observation for an EGS, is presented in Section 4. Finally, conclusions are stated in Section 5.

2 MODELING THE FLUID PRESSURE

We start by introducing some recurring notations. We denote reals, positive reals, and natural numbers (including 0) by $\mathbb{R}$, $\mathbb{R}_+$, and $\mathbb{N}$, respectively. Furthermore, we define $\mathbb{N}_{[i,k]} := \{j \in \mathbb{N} \,|\, i \leq j \leq k\}$. In addition to the Euclidean vector norm $\|x\|_2$, we frequently use $\|x\|_P := \sqrt{x^T P x}$, where P is a positive semi-definite square matrix. We write $\mathrm{diag}(d_1, \ldots, d_n)$ for a diagonal matrix with elements $d_1 \in \mathbb{R}$ through $d_n \in \mathbb{R}$ on its main diagonal. Finally, $\mathcal{N}(v, \varsigma^2)$ denotes a normal distribution with expectation $v \in \mathbb{R}$ and standard deviation $\varsigma \in \mathbb{R}_+$.

2.1 Diffusion equation and Darcy's law

The spatial and temporal evolution of the fluid pressure $p(\xi, t)$ in the reservoir can be approximated as a 1-dimensional hydraulically conductive system, which is described by the diffusion equation

$$\frac{\partial p(\xi,t)}{\partial t} = \frac{\kappa(\xi,t)}{\zeta\eta}\,\frac{\partial^2 p(\xi,t)}{\partial \xi^2}, \tag{1}$$

where ζ is the specific storage capacity, η is the fluid viscosity and κ is the (spatially and temporally varying) rock permeability (see, e.g., pp. 215 and 340 in Bear (1972) or Renner and Steeb (2014)). Using Darcy's law (see, e.g., p. 119 ff. in Bear (1972)), the injected and extracted fluid at the boundaries result in (Neumann) boundary conditions of the form

$$\frac{\partial p(0,t)}{\partial \xi} = -\frac{\eta\, q_{\text{in}}(t)}{S\,\kappa(0,t)} \quad \text{and} \quad \frac{\partial p(l,t)}{\partial \xi} = -\frac{\eta\, q_{\text{ex}}(t)}{S\,\kappa(l,t)}, \tag{2}$$

where S refers to the cross section of the reservoir (see Fig. 1). The initial-boundary value problem is completed by the initial condition $p(\xi, 0) = p^*$, where p^* is the hydrostatic fluid pressure depending on the depth of the reservoir.

2.2 Discretization

The partial differential equation (1) can be easily discretized using finite differences. However, considering that the permeability (and therefore the hydraulic diffusivity $\Lambda := \kappa/\zeta\eta$) varies in space and time, conventional forward Euler, backward Euler, or Crank-Nicolson schemes are not suitable. Following Eq. (7.9.8) in Bear (1972), we consequently use the adapted scheme

$$\sum_{\Delta j=-1}^{1} \alpha_{\Delta j}\, \frac{p_{j+\Delta j}^{k+1} - p_{j+\Delta j}^{k}}{\kappa_{j+\Delta j}^{k+1}\,\Delta t} = \sum_{\Delta k=0}^{1} \frac{p_{j-1}^{k+\Delta k} - 2\,p_{j}^{k+\Delta k} + p_{j+1}^{k+\Delta k}}{\zeta\,\eta\,\Delta\xi^2} \tag{3}$$

with the weighting coefficients

$$\alpha_{-1} := 1/6, \qquad \alpha_0 := 5/3, \quad \text{and} \quad \alpha_1 := 1/6,$$

where $p_j^k := p(\xi_j, t_k)$ and $\kappa_j^k := \kappa(\xi_j, t_k)$ with $\xi_j := j\Delta\xi$ and $t_k := k\,\Delta t$, and where $\Delta\xi$ and Δt denote the spatial and temporal step sizes, respectively. Clearly, (3) can only be applied to inner nodes of the discretization grid and thus does not apply for $j \in \{0, \nu\}$, where $\nu := l/\Delta\xi$. However, for the outer nodes, we obtain

$$q_i^k = \frac{S\,\kappa_0^{k+1}}{\eta}\,\frac{3\,p_0^{k+1} - 4\,p_1^{k+1} + p_2^{k+1}}{2\,\Delta\xi} \quad \text{and} \tag{4}$$

$$q_e^k = \frac{S\,\kappa_\nu^{k+1}}{\eta}\,\frac{-p_{\nu-2}^{k+1} + 4\,p_{\nu-1}^{k+1} - 3\,p_\nu^{k+1}}{2\,\Delta\xi} \tag{5}$$

by approximating (2) using a second-order difference quotient and by taking into account that $q_i(t)$ and $q_e(t)$ are constant in the time-interval $[t_k, t_{k+1})$. Equations (3), (4), and (5) can be summarized in the matrix equation

$$\Psi(\boldsymbol{\kappa}^{k+1})\,\boldsymbol{p}^{k+1} = \Phi(\boldsymbol{\kappa}^{k+1})\,\boldsymbol{p}^{k+1} + \Upsilon(\boldsymbol{\kappa}^{k+1})\,\boldsymbol{q}^k, \tag{6}$$

where $\Psi, \Phi \in \mathbb{R}^{(\nu+1)\times(\nu+1)}$, $\Upsilon \in \mathbb{R}^{(\nu+1)\times 2}$, and

$$\boldsymbol{\kappa}^k := \begin{pmatrix} \kappa_0^k \\ \vdots \\ \kappa_\nu^k \end{pmatrix}, \quad \boldsymbol{p}^k := \begin{pmatrix} p_0^k \\ \vdots \\ p_\nu^k \end{pmatrix}, \quad \text{and} \quad \boldsymbol{q}^k := \begin{pmatrix} q_{\text{in}}^k \\ q_{\text{ex}}^k \end{pmatrix}.$$

2.3 Fracturing and seismic events

Hydraulic stimulation can cause seismic events (see, e.g, McGarr (2014)). The occurrence of an injection-induced seismic event is generally understood to result from a reduction of the effective normal stress due to the increase in fluid pressure on pre-existing faults to the point where their stress states reach the critical condition for frictional failure (cf. Baisch et al. (2010)). We discretize the shear stress profile using the same spatial grid as for the discretization of the diffusion equation. We associate the shear stress $\tau_j^k := \tau(\xi_j, t_k)$ with every point on the discretization grid. A seismic event occurs around a grid point, if the condition

$$\mu\,(\sigma - p_j^k) < \tau_j^k \tag{7}$$

holds, where μ is the friction coefficient and where σ denotes the (constant) normal stress (cf. Eq. (1) in Baisch et al. (2010)). A seismic event is assumed to have two side effects. First, the stress field will locally change. More precisely, the stress τ_j^k will be reduced by an uncertain amount $\Delta\tau$ and some of the released stress will be transferred to neighboring regions. Second, the permeability κ_j^k will be increased by a factor $(1+\epsilon)$, where ϵ is again uncertain. The stress transfer may cause elements to satisfy condition (7) for which we initially found $\mu\,(\sigma - p_j^k) \geq \tau_j^k$. This behavior may lead to chain reactions and thus may result in major seismic events (see Bak and Tang (1989) and Miller et al. (1996)). Formally, the shear stress and permeability update from time t_k to t_{k+1} can be described by the following algorithm, which is inspired by the procedure in Sect. 3 in Baisch et al. (2010).

Algorithm 1: Pressure, stress and permeability update.

1. Set $\mathcal{J} \leftarrow \emptyset$, $\boldsymbol{\kappa}^{k+1} \leftarrow \boldsymbol{\kappa}^k$, and $\boldsymbol{\tau}^{k+1} \leftarrow \boldsymbol{\tau}^k$.
2. Generate $\epsilon \sim \mathcal{N}(\hat{\epsilon}, \varsigma_\epsilon^2)$ and $\Delta\tau \sim \mathcal{N}(\Delta\hat{\tau}, \varsigma_{\Delta\tau}^2)$.
3. Repeat the following steps until $\Delta\mathcal{J} = \emptyset$.

(a) Set $\Delta\mathcal{J} \leftarrow \{j \in \mathbb{N}_{[0,\nu]} \setminus \mathcal{J} \mid (7) \text{ holds}\}$.

(b) For every $j \in \Delta\mathcal{J} \setminus \{0, \nu\}$, set $\tau_{j-1}^{k+1} \leftarrow \tau_{j-1}^{k+1} + 0.45\,\Delta\tau$, $\tau_j^{k+1} \leftarrow \tau_j^{k+1} - \Delta\tau$, and $\tau_{j+1}^{k+1} \leftarrow \tau_{j+1}^{k+1} + 0.45\,\Delta\tau$.

(c) For every $j \in \Delta\mathcal{J} \cap \{0, \nu\}$, set $\tau_j^{k+1} \leftarrow \tau_j^{k+1} - 0.6\,\Delta\tau$ and $\tau_{|j-1|}^{k+1} \leftarrow \tau_{|j-1|}^{k+1} + 0.45\,\Delta\tau$.

(d) For every $j \in \Delta\mathcal{J}$, set $\kappa_j^{k+1} \leftarrow (1+\epsilon)\,\kappa_j^{k+1}$.

(e) Set $\mathcal{J} \leftarrow \mathcal{J} \cup \Delta\mathcal{J}$.

4. Set $s^{k+1} \leftarrow |\mathcal{J}|$ and compute $\mathbf{p}^{k+1}$ according to (6).

Step 3.(b) describes the stress transfer. Similar to Figure 4 inBaisch et al. (2010), we assume that $90\% = 2 \cdot 45\%$ of the stress reduction $\Delta\tau$ is transferred to the two neighboring regions. Step 3.(c) uses an adapted stress transfer to account for boundary effects. Now, after evaluating step 3 in Algorithm 1, the set $\mathcal{J}$ contains the indices j of all locations ξ_j, where seismic events occur in the time interval $[t_k, t_{k+1})$. The seismic moment roughly is proportional to the slip-plane area. Thus, in our model, $|\mathcal{J}|$ provides a measure of the strength of the seismic event, which we store in the variable $s^k := s(t_k)$.

2.4 Model parameters

The choice for the various model parameters (see Table 2) does not intend to represent a specific geothermal site. However, the assumed size and depth of the reservoir, the stress field, and the rock and fluid parameters roughly match the conditions at Soultz-sous-Forêts (cf. Tab. 2 in Baisch et al. (2010)). The spatial step size is chosen such that $l/\Delta\xi \in \mathbb{N}$. In fact, we have $\nu := l/\Delta\xi = 120$.

Table 2: Model parameters.

Parameter	Symbol	Value	Unit
reservoir length	l	600	m
reservoir cross section	S	5000	m^2
storage coefficient	ζ	10^{-9}	$1/\text{Pa}$
fluid viscosity	η	$2.4 \cdot 10^{-4}$	Pa s
initial rock permeability	κ^*	$2 \cdot 10^{-14}$	m^2
initial fluid pressure	p^*	48	MPa
temporal step size	Δt	5	s
spatial step size	$\Delta\xi$	5	m
normal stress	σ	79	MPa
friction coefficient	μ	0.8	1
permeability update	$\hat{\epsilon}$	0.02	1
permeability uncertainty	ς_ϵ	0.002	1
shear stress update	$\Delta\hat{\tau}$	0.8	MPa
shear stress uncertainty	$\varsigma_{\Delta\tau}$	0.02	MPa

3 MODEL ANALYSIS

The model introduced in Sect. 2 can be understood as a nonlinear state space model with uncertainty. Introducing the state and input vectors

$$x(t_k) = \begin{pmatrix} \boldsymbol{p}^k \\ \boldsymbol{\kappa}^k \\ \boldsymbol{\tau}^k \\ s^k \end{pmatrix} \in \mathbb{R}^{364} \quad \text{and} \quad u(t_k) = \boldsymbol{q}^k \in \mathbb{R}^2,$$

respectively, the transition from $x(t_k)$ to $x(t_{k+1})$ can be written as

$$x(t_{k+1}) = f(x(t_k), u(t_k), v(t_k)), \tag{8}$$

where v represents the uncertain variables ϵ and $\Delta\tau$ from step 2 in Algorithm 1. The function f is in general not differentiable (due to the switching behavior of the system resulting from step 3 in Alg. 1). The output of the system is defined with respect to the pressure control designed in Section 4. Since the control scheme only accounts for the pressures at the locations $\xi_{20(i-1)+1}$ with $i \in \mathbb{N}_{[1,7]}$, we introduce the system output $y(t_k) = C_y\,x(t_k)$ with

$$C_y := \sum_{i=1}^{7} e_i\,\varepsilon_{20(i-1)+1}^T \in \mathbb{R}^{7\times 364},$$

where $e_i \in \mathbb{R}^7$ and $\varepsilon_j \in \mathbb{R}^{364}$ are Cartesian unit vectors. Note that y_1 and y_7 refer to the bottomhole pressures in the two wells, i.e., at $\xi = 0\,\mathrm{m}$ and $\xi = 600\,\mathrm{m}$. Obviously, the nonlinear uncertain system becomes linear and deterministic if steps 2 and 3 are skipped in Algorithm 1. In fact, in this case, f from (8) can be rewritten as

$$f(x, u, v) = A\,x + B\,u \tag{9}$$

with appropriate matrices $A \in \mathbb{R}^{364\times364}$ and $B \in \mathbb{R}^{364\times2}$ (to be specified further below). We will make use of the linear approximation[1] to predict the system behavior within the MPC in Section 4.

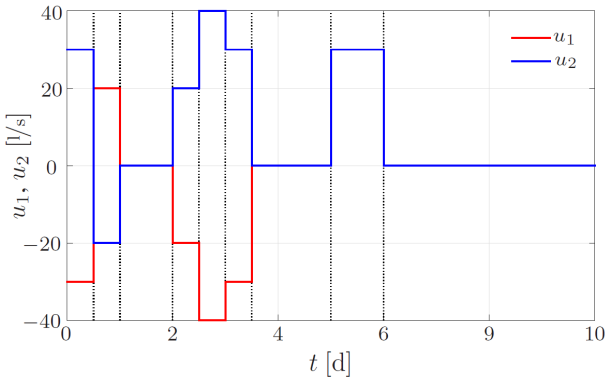

Figure 2: Test inputs for the analysis of the models.

As a preparation for the controller design, we analyze the response of the nonlinear system and the linear approximation for the test inputs depicted in Figure 2. The input signals satisfy $u_1(t) = -u_2(t)$ for every $t \in [0\,\mathrm{d}, 5\,\mathrm{d}]$ and $u_1(t) = u_2(t)$ for every $t \in (5\,\mathrm{d}, 10\,\mathrm{d}]$. The evolution of the corresponding pressures y_1 and y_5 at $\xi = 0\,\mathrm{m}$ and $\xi = 400\,\mathrm{m}$ are qualitatively comparable for the nonlinear model with uncertainty and the linear deterministic one (see Figs. 3 and 4).

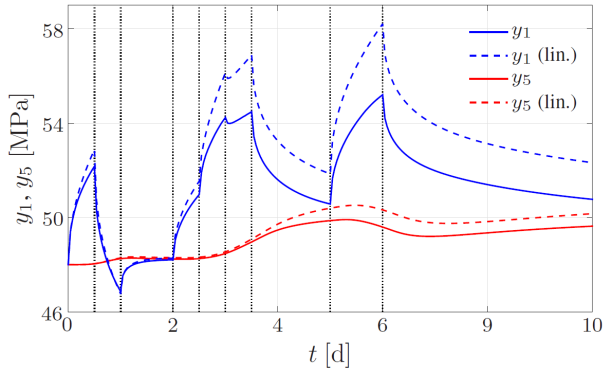

Figure 3: Outputs of the linear and nonlinear model for the test inputs shown in Figure 2.

More important, both models show typical characteristics of EGS. In fact, the pressure y_1 at the injection reacts immediately and intensely to changes of the flow rate. In contrast, the pressure y_5 in the reservoir (at $\xi = 400\,\mathrm{m}$) shows a delayed and damped reaction due to diffusion.

[1]Clearly, only the states related to the pressures $\boldsymbol{p}^k$ change in the linear model. We thus could eliminate the remaining $364 - 121 = 243$ states without loosing information. This observation is, however, only important for the numerical evaluation of the MPC in Section 4.

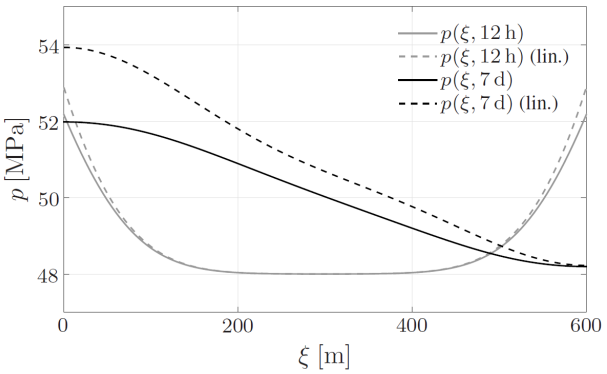

Figure 4: Pressure profiles of the linear and nonlinear model for the test inputs shown in Fig. 2.

Moreover, the largest seismic event occurs (shortly) *after* the time interval $[60\,\mathrm{h}, 72\,\mathrm{h}]$ with the highest injection rate (see Fig. 5). This so-called post-injection seismicity (see, e.g., Sect. 5.4 in Baisch et al. (2010)) is typical for hydraulic stimulations in EGS.

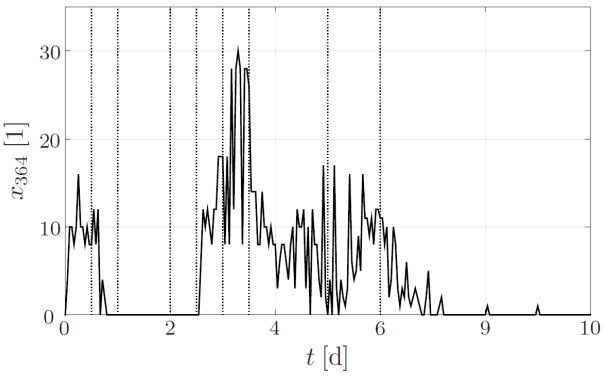

Figure 5: The strongest seismic event per hour (of the nonlinear model) for the test inputs shown in Figure 2.

4 PREDICTIVE PRESSURE CONTROL

We now introduce the predictive control scheme to regulate the fluid pressure in the deep geothermal system. In particular, we intend to control the system such that

$$\lim_{t\to\infty} y_2(t) = \breve{y}_2 \quad \text{and} \quad \lim_{t\to\infty} y_5(t) = \breve{y}_5, \tag{10}$$

where $\breve{y}_2$ and $\breve{y}_5$ are user-defined reference values for the pressures at $\xi = 100\,\mathrm{m}$ and $\xi = 400\,\mathrm{m}$, respectively. Since flow rates and pressures in the wells are limited, we additionally require input and output constraints of the form $\underline{u} \le u(t) \le \overline{u}$ and $\underline{y} \le y(t) \le \overline{y}$ to be satisfied (at least point-wise in time). Clearly, the described control task does not exactly match the situation in practical application. However, in this study, we are mainly interested in presenting a first approach for predictive pressure control in deep geothermal systems.

4.1 MPC with linear prediction

The control task can be intuitively formulated in the framework of MPC (see Rawlings and Mayne (2009)).

The associated OCP (with a structure similar to Eq. (11) below) may, however, be hard to solve for naive implementations. First, the usage of the nonlinear uncertain model to predict the system behavior results in a non-convex optimization problem. Second, the high number of states implies a high number of equality constraints (which could, of course, be eliminated). Third, the slow dynamics of the system (apparent from Fig. 3) require long prediction horizons resulting in a high number of decision variables.

We make some simplifications to facilitate the numerical solution of the OCP. First, we use a linear approximation of the nonlinear prediction model. Regarding the analysis in Section 3, this simplification is justifiable for moderate prediction horizon lengths. Second, we apply a quadratic performance index. As a consequence, the OCP can be rewritten as a quadratic program (QP). Third, we (later) eliminate equality constraints to reduce the number of constraints. Fourth, we employ move blocking strategies (see, e.g., Cagienard et al. (2004)) to reduce the number of decision variables. In particular, we assume that the inputs only change every $M \in \mathbb{N}$ time steps (i.e., $u(t_{Mi+k}) = u(t_{Mi})$ for every $i \in \mathbb{N}$ and $k \in \mathbb{N}_{[1,M-1]}$). Moreover, we require the output constraints to be fulfilled only at the times t_{Mi} for $i \in \mathbb{N}$. In summary, we consider the MPC scheme

$$
\begin{aligned}
V(x^*) := \min_{\boldsymbol{u},\boldsymbol{x},\boldsymbol{y}} \; & \sum_{i=1}^{N_y} \|y(t_{Mi}) - \breve{y}\|_Q^2 + \sum_{i=0}^{N_u-1} \|u(t_{Mi}) - \breve{u}\|_R^2 \\
\text{s.t.} \quad & x(t_0) = x^*, && (11)\\
& x(t_{k+1}) = A^* x(t_k) + B^* u(t_k), && \forall k \in \mathbb{N}_{[0,MN_y-1]},\\
& y(t_{Mi}) = C_y\, x(t_{Mi}), && \forall i \in \mathbb{N}_{[1,N_y]},\\
& u(t_{Mi}) = u(t_{M(N_u-1)}), && \forall i \in \mathbb{N}_{[N_u,N_y-1]},\\
& u(t_{Mi+k}) = u(t_{Mi}),\ \forall i \in \mathbb{N}_{[0,N_y-1]}, && \forall k \in \mathbb{N}_{[1,M-1]},\\
& \underline{u} \le u(t_{Mi}) \le \overline{u}, && \forall i \in \mathbb{N}_{[0,N_u-1]},\\
& \underline{y} \le y(t_{Mi}) \le \overline{y}, && \forall i \in \mathbb{N}_{[1,N_y]},
\end{aligned}
$$

where N_y and N_u refer to the output and input prediction horizon, respectively. The vectors $\breve{y} \in \mathbb{R}^7$ and $\breve{u}$ denote the output and input references. The positive (semi-) definite matrices Q and R weight the differences between the predicted output and input trajectories and the corresponding reference values. Finally, inspired by (6) and (9), the linearization around the initial condition x^* is described by the matrices

$$
A^* := \begin{pmatrix} \Psi^{-1}(\boldsymbol{\kappa}^*)\,\Phi(\boldsymbol{\kappa}^*) & 0 \\ 0 & I_{243} \end{pmatrix} \quad \text{and}
$$

$$
B^* := \begin{pmatrix} \Psi^{-1}(\boldsymbol{\kappa}^*)\,\Upsilon(\boldsymbol{\kappa}^*) \\ 0 \end{pmatrix},
$$

where $\boldsymbol{\kappa}^* := \begin{pmatrix} x^*_{122} & \dots & x^*_{242} \end{pmatrix}^T$. The OCP (11) is solved by choosing the decision variables

$$
\boldsymbol{u} := \begin{pmatrix} u(t_0) \\ u(t_1) \\ \vdots \\ u(t_{MN_y-1}) \end{pmatrix},\ \boldsymbol{x} := \begin{pmatrix} x(t_0) \\ x(t_1) \\ \vdots \\ x(t_{MN_y}) \end{pmatrix},\ \boldsymbol{y} := \begin{pmatrix} y(t_M) \\ y(t_{2M}) \\ \vdots \\ y(t_{MN_y}) \end{pmatrix}
$$

such that the cost in (11) is minimized. The value $V(x^*)$ is the optimal cost for the initial state x^*. Now, by eliminating all equality constraints according to the procedure in Bemporad et al. (2002), (11) can be equivalently rewritten as the QP

$$
\begin{aligned}
V(x^*) = \min_{\boldsymbol{z}} \; & \frac{1}{2}\,\boldsymbol{z}^T H\,\boldsymbol{z} + (Gx^* + g)^T \boldsymbol{z} + \|Fx^* + c\|_2^2 \\
\text{s.t.} \quad & E\,\boldsymbol{z} \le D\,x^* + d && (12)
\end{aligned}
$$

with appropriate matrices (and vectors) H, G, g, F, E, D, d, and c (see Bemporad et al. (2002) for details) and the decision variables

$$
\boldsymbol{z} := \begin{pmatrix} u(t_0) \\ u(t_M) \\ \vdots \\ u(t_{M(N_u-1)}) \end{pmatrix} \in \mathbb{R}^{2N_u}. \qquad (13)
$$

During runtime of the controller, the OCP (12) (or, alternatively (11)) is repeatedly solved for the current state x^* and the first element of the optimal input sequence is applied to the system. Formally, this procedure leads to the control law

$$
\varrho(x^*) := u^*(t_0),
$$

where $u^*(t_0)$ is the first entry of the optimizer $\boldsymbol{z}^*$ for (12) at x^*.

It remains to specify the choice of the weighing matrices and the reference signals. Regarding the control task in (10), the choice $Q = e_2\,e_2^T + e_5\,e_5^T \in \mathbb{R}^{7\times 7}$ is suitable to penalize deviations from the output references $\breve{y}_2$ and $\breve{y}_5$ as specified in Eq. (10). Clearly, this choice of Q implies that the deviations $y_j(t) - \breve{y}_j$ for $j \in \mathbb{N}_{[1,7]} \setminus \{2,5\}$ do not influence the performance index. Consequently, $\breve{y} := \breve{y}_2\,e_2 + \breve{y}_5\,e_5 \in \mathbb{R}^7$ is a suitable choice for the output reference. An appropriate choice for the input reference requires some preparation. Obviously, the inputs $\breve{u}$ should support stationarity of the system if $y_2(t^*) = \breve{y}_2$ and $y_5(t^*) = \breve{y}_5$ hold for some $t^* \in \mathbb{R}_+$. From (1), we infer that stationarity requires

$$
0 = \frac{\partial^2 p(\xi, t^*)}{\partial \xi^2} \qquad \text{for every} \qquad \xi \in [0, l], \qquad (14)
$$

which can only be fulfilled if $p(\xi, t^*)$ is affine. By definition of the system outputs y, we have $y_2(t^*) = p(100, t^*)$ and $y_5(t^*) = p(400, t^*)$. Thus, the affine pressure profile is uniquely defined by $\breve{y}_2$ and $\breve{y}_5$. In fact, $p(\xi, t^*)$ can be written as $p(\xi, t^*) = a\,\xi + b$ with

$$
a := \frac{\breve{y}_5 - \breve{y}_2}{300} \qquad \text{and} \qquad b := \frac{4\,\breve{y}_2 - \breve{y}_5}{3}.
$$

We thus require the injection and extraction flow rates

$$
q_{\text{in}}(t^*) = -\frac{S\,a}{\eta}\,\kappa(0, t^*) \quad \text{and} \quad q_{\text{ex}}(t^*) = -\frac{S\,a}{\eta}\,\kappa(l, t^*)
$$

to ensure stationarity (see (2)). Now, assuming that the permeability does not change in the future (which is, by

definition, true for a stationary state), we choose the input references

$$\breve{u}_1 := -\frac{S\,a}{\eta}\,x^*_{122} \qquad \text{and} \qquad \breve{u}_2 := -\frac{S\,a}{\eta}\,x^*_{242} \quad (15)$$

depending on the current state x^*. Finally, we choose the input weighting $R = r\,I_2$, where $r \in \mathbb{R}_+$ is a tuning parameter.

4.2 UKF with nonlinear prediction

The application of the introduced MPC scheme requires (an estimation of) the current system state x^*. Clearly, it is not feasible to measure the complete profiles of pressure, permeability, and shear stress in the reservoir. In fact, very few measurements can be realized in practice. Here, we assume that the fluid pressures in both wells, i.e., $p(\xi_0, \cdot) = x_1$ and $p(\xi_\nu, \cdot) = x_{121}$ are measured. Moreover, we assume that the current magnitude of the seismic events is accessible via $s = x_{364}$. This assumption is reasonable since the induced seismicity is usually tracked during hydraulic stimulations (see, e.g., Sect. 2 in Baisch et al. (2010), or Le Calvez et al. (2007)). All measurements are, however, affected by noise. Specifically, we assume that the measurements $m(t_k) \in \mathbb{R}^3$ at time t_k are described by

$$m(t_k) = C_m\,x(t_k) + w(t_k)$$

where $C_m := e_1\,\varepsilon_1^T + e_2\,\varepsilon_{121}^T + e_3\,\varepsilon_{364}^T \in \mathbb{R}^{3\times 364}$ and where $w_1 \sim \mathcal{N}(0, \varsigma_p^2)$, $w_2 \sim \mathcal{N}(0, \varsigma_p^2)$, and $w_3 \sim \mathcal{N}(0, \varsigma_s^2)$.

Many methods exist that compute an estimate $\hat{x}^*$ of the current state x^* given an estimation of the former state $\hat{x}^-$, the former input u^-, and the current (noisy) measurement m^*. Here, we design a UKF (see, e.g., Julier and Uhlmann (1997) or Wan and van der Merwe (2000)) to observe the system state. The UKF is capable of handling nonlinear uncertain systems with non-differentiable functions f. Moreover, it can be applied to large-scale systems since the estimation procedure builds on a small number of test (or sigma) points (compared to particle filters as in, e.g., Arulampalam et al. (2002)). The UKF is thus a well-suited choice for the system described in Section 2. To handle the uncertainties, the UKF exploits information on the distribution of the uncertain variables. In particular, we require (estimations of) the mean $\hat{v}$ and the covariance matrix P_{vv} of the process uncertainty v as well as the covariance matrix P_{ww} of the measurement noise. Obviously, based on the assumed distributions of v and w, we have $\hat{v} = \begin{pmatrix}\hat{\epsilon} & \Delta\hat{\tau}\end{pmatrix}^T$, $P_{vv} = \mathrm{diag}(\varsigma_\epsilon^2, \varsigma_{\Delta\tau}^2)$, and $P_{ww} = \mathrm{diag}(\varsigma_p^2, \varsigma_p^2, \varsigma_s^2)$. The UKF can now be implemented according to Algorithm 2, which is based on Box 3.1 in Julier and Uhlmann (1997) and Alg. 3.1 inWan and van der Merwe (2000). As a preparation, we define the weighting coefficients

$$\beta_0 := \frac{\lambda}{366+\lambda} \qquad \text{and} \qquad \beta_i := \frac{1}{2\,(366+\lambda)} \quad (16)$$

for every $i \in \mathbb{N}_{[1,732]}$ and some $\lambda \in \mathbb{R}$ (with $\lambda \neq -366$). Thereby, $366 = 364 + 2$ refers to the dimension of the augmented state vector that concatenates the original state and the process noise (see Eq. (15) in Julier and Uhlmann (1997)). In addition to the weighting coefficients, we precalculate the v coordinates[2] of the $733 = 2\cdot 366 + 1$ sigma points according to $\mathcal{V}_i := \hat{v}$ for every $i \in \mathbb{N}_{[0,728]}$ as well as

$$\mathcal{V}_{728+i} := \hat{v}^- + \sqrt{366+\lambda}\,e_i^T L_v \qquad \text{and}$$
$$\mathcal{V}_{730+i} := \hat{v}^- - \sqrt{366+\lambda}\,e_i^T L_v$$

for every $i \in \{1, 2\}$, where $L_v := \mathrm{diag}(\varsigma_\epsilon, \varsigma_{\Delta\tau})$. Note that L_v obeys $L_v L_v^T = P_{vv}$. Now, Algorithm 2 first computes the x coordinates of the 733 sigma points. In step 2, the nonlinear model is used to compute state and output predictions for every sigma point (with the components $\mathcal{X}_i^-$ and $\mathcal{V}_i$). In step 3 and 4, these predictions are used to calculate the expectations for the current state and output, and the covariance matrices $\tilde{P}_{xx}$, P_{xm}, and P_{mm}, respectively. Finally, in step 5, the filter gain W is computed, which is used to adapt the estimations for the current state and the associated covariance matrix.

Algorithm 2: UKF implementation.

1. Compute L_x such that $L_x L_x^T = P_{xx}^-$ and set sigma points as follows.

(a) For every $i \in \{0\} \cup \mathbb{N}_{[729,732]}$, set $\mathcal{X}_i^- \leftarrow \hat{x}^-$.

(b) For every $i \in \mathbb{N}_{[1,364]}$, set
$\mathcal{X}_i^- \leftarrow \hat{x}^- + \sqrt{366+\lambda}\,\varepsilon_i^T L_x$ and
$\mathcal{X}_{364+i}^- \leftarrow \hat{x}^- - \sqrt{366+\lambda}\,\varepsilon_i^T L_x$.

2. For every $i \in \mathbb{N}_{[0,732]}$, compute predictions
$\mathcal{X}_i \leftarrow f(\mathcal{X}_i^-, u^-, \mathcal{V}_i)$ and $\mathcal{M}_i \leftarrow C_m\,\mathcal{X}_i$.
3. Compute $\tilde{x} \leftarrow \sum_{i=0}^{732} \beta_i \mathcal{X}_i$ and $\tilde{m} \leftarrow \sum_{i=0}^{732} \beta_i \mathcal{M}_i$.
4. Compute approximations of covariance matrices.

(a) $\widetilde{P}_{xx} \leftarrow \sum_{i=0}^{732} \beta_i (\mathcal{X}_i - \tilde{x})\,(\mathcal{X}_i - \tilde{x})^T$.

(b) $P_{xm} \leftarrow \sum_{i=0}^{732} \beta_i (\mathcal{X}_i - \tilde{x})\,(\mathcal{M}_i - \tilde{m})^T$.

(c) $P_{mm} \leftarrow P_{ww} + \sum_{i=0}^{732} \beta_i (\mathcal{M}_i - \tilde{m})\,(\mathcal{M}_i - \tilde{m})^T$.

5. Compute filter gain $W \leftarrow P_{xm}\,P_{mm}^{-1}$ and set
$\hat{x}^* \leftarrow \tilde{x} + W(m^* - \tilde{m})$ and $P_{xx} \leftarrow \widetilde{P}_{xx} - W P_{mm} W^T$.

We stress that the choice of the weighting coefficients in (16) refers to the *unscaled* unscented transformation as introduced in Eq. (12) in Julier and Uhlmann (1997). The performance of the UKF can often be improved by considering the *scaled* unscented transformation as discussed in Julier (2002) and applied in Eq. (15) in Wan and van der Merwe (2000). Here, we do not make use of this improvement to keep the number of observer parameters at a minimum (i.e., only λ).

4.3 Combination and simulation

We briefly explain the combination of the controller (i.e., the MPC) and the observer (i.e., the UKF) for the system of interest (i.e., the EGS). The MPC generates the

[2] Neglecting a potential covariance between the state estimation and the process uncertainty, the sigma points in the augmented space can be computed independently in the x and v coordinates.

input u based on the output reference, the (current) input reference, and the estimation of the current system state (see Fig. 6). According to (15), the input reference is not a design parameter since it depends on (an approximation of) the current system state. Now, the UKF estimates $\hat{x}$ based on the input u and the (noisy) measurements m (see Alg. 2). The sampling time of the observer is chosen to equal the temporal step size Δt of the model. In contrast, the controller is only evaluated every M time steps following the move blocking strategy in Section 4.1.

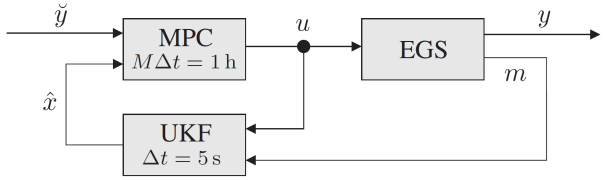

Figure 6: Illustration of the control loop with sampling times of the controller and observer.

We implemented the controller and observer using the parameters in Table 3. With Δt and M as in Tables 2 and 3, the sampling times of the controller and the observer thus are $M\,\Delta t = 3600\,\mathrm{s} = 1\,\mathrm{h}$ and $\Delta t = 5\,\mathrm{s}$, respectively. In addition, the choice $N_y = 72$ implies that the outputs are predicted for $N_y M \Delta t = 3\,\mathrm{d}$. Moreover, the input prediction horizon $N_u = 24$ sets the number of decision variables equal to 48 (see Eq. (13)). Regarding the observer, we found $\lambda = 50$ to be suitable to describe the unscented transformation. Finally, we randomly initialized the observer state $\hat{x}(t_0)$ in the hyperrectangle $[0.98, 1.02]\,x(t_0)$, i.e., with a maximum relative error of 2%.

Table 3: Controller and observer parameters.

Parameter	Symbol	Value	Unit
first reference pressure	$\breve{y}_2$	57	MPa
second reference pressure	$\breve{y}_5$	50	MPa
output prediction horizon	N_y	72	1
input prediction horizon	N_u	24	1
maximum injection rate	$\overline{u}_1$	40	l/s
minimum injection rate	$\underline{u}_1$	−30	l/s
maximum production rate	$\overline{u}_2$	30	l/s
minimum production rate	$\underline{u}_2$	−40	l/s
maximum pressure	$\overline{y}_1, \ldots, \overline{y}_7$	70	MPa
minimum pressure	$\underline{y}_1, \ldots, \underline{y}_7$	44	MPa
sample time multiplier	M	720	1
pressure noise	ς_p	0.2	MPa
seismicity noise	ς_s	0.5	1
observer parameter	λ	50	1

The resulting control scheme is capable of solving the considered control task. As apparent from Figure 8, the control inputs in Figure 7 realize the desired pressures at the positions $\xi = 100\,\mathrm{m}$ and $\xi = 400\,\mathrm{m}$. In fact, the reference pressures are matched after $t \approx 6\,\mathrm{d}$ without violating the input and state constraints. Moreover, as expected, the pressure profile tends to the affine profile determined by $\breve{y}_2$ and $\breve{y}_5$ for $t \to \infty$ (see Fig. 9).

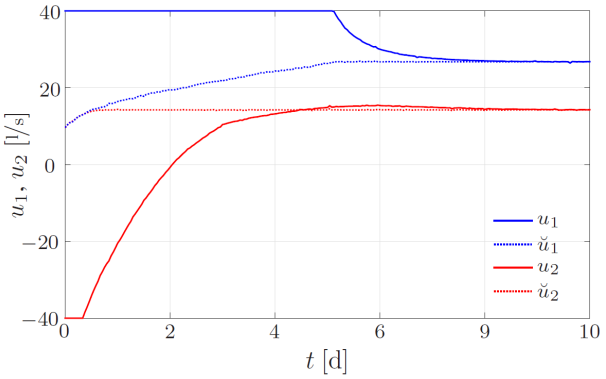

Figure 7: Inputs of the controlled system.

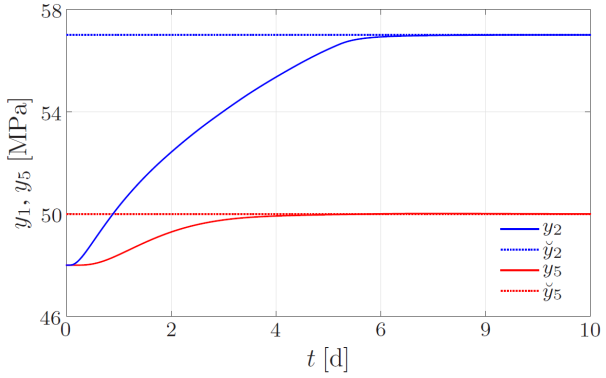

Figure 8: Outputs of the controlled system.

As illustrated in Figure 10, the state transition causes a number of seismic events. Since seismicity involves permeability increases, the hydraulic diffusity changes continuously. These (inhomogeneous) changes in permeability also explain that the injected and extracted fluid flows do not match for $t \to \infty$. In fact, taking the reference inputs (15) into account, the mismatch is obviously caused by different permeabilities around the injection and production well.

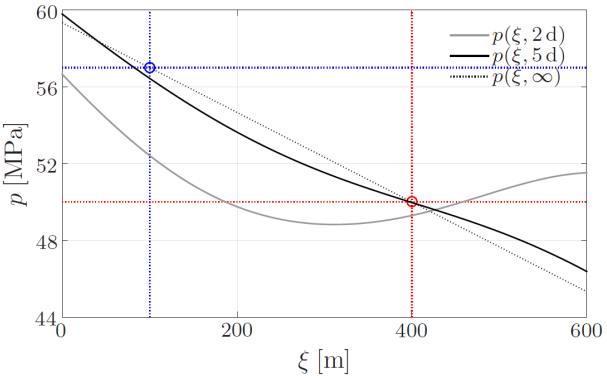

Figure 9: Pressure profiles of the controlled system.

Finally, it remains to evaluate the performance of the observer. Obviously, the estimated seismic activity $\hat{x}_{364}$

well matches the actual seismicity (see Fig. 10). The quality of the estimation for the remaining states can be analyzed by means of the error

$$E(t_k) := \|x(t_k) - \hat{x}(t_k)\|_2. \tag{17}$$

The observer reliably reconstructs the system states based on the available measurements (see Fig. 11).

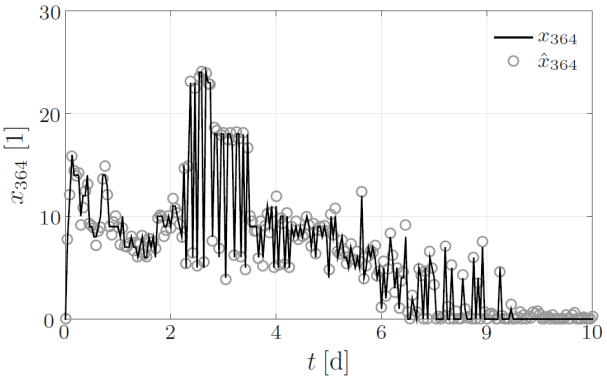

Figure 10: The strongest seismic event per hour of the simulated controlled system and the estimated counterpart provided by the observer.

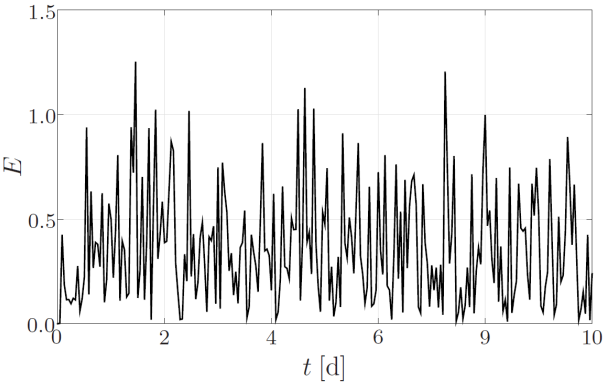

Figure 11: State estimation errors (as in Eq. (17)**) at sampling instances of the controller.**

5 CONCULUSION AND OUTLOOK

We presented a predictive control scheme for the regulation of the fluid pressure profile in deep geothermal systems during hydraulic stimulation. The MPC builds on a rudimentary model (inspired by Baisch et al. (2010)) describing the pressurization and seismicity in the reservoir. Since only the fluid pressure in the two wells as well as the seismic activity can be measured directly, a UKF was designed to solve the observation problem. Numerical simulations showed the effectiveness of the approach.

During hydraulic stimulations of reservoir rocks, one intends to avoid strong seismic events since geothermal sites are often located in the proximity of populated areas. Controlling the fluid pressure profile in the reservoir is a first step in this direction. Nevertheless, future work has to address the explicit inclusion of seismic activity in the predictive control scheme. This extension is nontrivial, since the linear approximation (currently used in the MPC), does not incorporate seismicity. Clearly, the nonlinear uncertain model can instead be used to predict the system behavior. However, doing so leads to a large-scale non-convex OCP that we cannot solve efficiently so far.

ACKNOWLEDGMENT

Partial funding by the German Research Foundation (DFG) under the grants SCHU 2094/1-1 and SCHU 2094/2-1 is gratefully acknowledged.

REFERENCES

Arulampalam, M. S., Maskell, S., Gordon, N., and Clapp, T. A tutorial on particle filters for online nonlinear/non-Gaussian Bayesian tracking. *IEEE Transactions on Signal Processing*, 50(2):174–188, 2002.

Baisch, S., Vörös, R., Rothert, E., Stang, H., Jung, R., and Schellschmidt, R. A numerical model for fluid injection induced seismicity at Soultz-sous-Fôret. *International Journal of Rock Mechanics and Mining Sciences*, 47:405–413, 2010.

Bak, P. and Tang, C. Earthquakes as a self-organized critical phenomenon. *Journal of Geophysical Research*, 94 (B 11):15635–15637, 1989.

Bear, J. *Dynamics of Fluids in Porous Media*. Dover Publications, 1972.

Bemporad, A., Morari, M., Dua, V., and Pistikopoulos, E. N. The explicit linear quadratic regulator for constrained systems. *Automatica*, 38(1):3–20, 2002.

Bertani, R. Geothermal power generation in the world 2010–2014 update report. In *Proc. of the World Geothermal Congress 2015*, 2015.

Bommer, J. J., Oates, S., Cepeda, J. M., Lindholm, C., Bird, J., Torres, R., Marroquín, G., and Rivas, J. Control of hazard due to seismicity induced by a hot fractured rock geothermal project. *Engineering Geology*, 83:287–306, 2006.

Bönnemann, C., Schmidt, B., Ritter, J., Gestermann, N., Plenefisch, T., and Wegler, U. Das seismische Ereignis bei Landau vom 15. August 2009. Abschlussbericht der Expertengruppe “Seismisches Risiko bei hydrothermaler Geothermie”, 2010.

Cagienard, R., Grieder, P., Kerrigan, E. C., and Morari, M. Move blocking strategies in receding horizon control. In *Proc. of 43rd IEEE Conference on Decision and Control*, pages 2023–2028, 2004.

Evans, K. E., Zappone, A., Kraft, T., Deichmann, N., and Moia, F. A survey of the induced seismic responses to fluid injection in geothermal and CO_2 reservoirs in europe. *Geothermics*, 41:30–54, 2012.

Gaucher, E., Schoenball, M., Heidbach, O., Zang, A., Fokker, P. A., Wees, J.-D., and Kohl, T. Induced

seismicity in geothermal reservoirs: A review of forecastingapproaches. *Renewable and Sustainable Energy Reviews*, 52:1473–1490, 2015.

Häring, M. O., Schanz, U., Ladner, F., and Dyer, B. C. Characterisation of the Basel 1 enhanced geothermal system. *Geothermics*, 37:469–495, 2008.

Julier, S. J. The scaled unscented transformation. In *Proc. of the American Control Conference*, pages 4555–4559, 2002.

Julier, S. J. and Uhlmann, J. K. New extension of the Kalman filter to nonlinear systems. In *Proc. of the 11th Symposin on Aerospace / Defence Sensing, Simulation, and Controls*, 1997.

Le Calvez, J. H., Craven, M. E., Klem, R. C., Baihly, J. D., Bennett, L. A., and Brook, K. Real-time microseismic monitoring of hydraulic fracture treatment: A tool to improve completion and reservoir management. In *Proc. of the SPE Hydraulic Fracturing Technology Conference*, 2007.

McGarr, A. Maximum magnitude earthquakes induced by fluid injection. *J. Geophys. Res. Solid Earth*, 119: 1008–1019, 2014.

Miller, S. A., Nur, A., and Olgaard, D. L. Earthquakes as a coupled shear stress - high pore pressure dynamical system. *Geophysical Research Letters*, 23(2):197–200, 1996.

Rawlings, J. B. and Mayne, D. Q. *Model Predictive Control: Theory and Design*. Nob Hill Publishing, 2009.

Renner, J. and Steeb, H. Modeling of fluid transport in geothermal research. In *Handbook of Geomathematics*, pages 1–55. Springer, 2014.

Schulze Darup, M. and Renner, J. Predictive pressure control of deep geothermal systems. In *Proc. of the European Control Conference*, 2016.

Wan, E. A. and van der Merwe, R. The unscented Kalman filter for nonlinear estimation. In *Proc. of the IEEE 2000 Adaptive Systems for Signal Processing, Communications, and Control Symposium*, pages 153–158, 2000.